Forcing of Low-Frequency Ocean Variability in the Northeast Pacific*

Kettyah C. Chhak and Emanuele Di Lorenzo

School of Earth and Atmospheric Sciences, Georgia Institute of Technology, Atlanta, Georgia

Niklas Schneider

Department of Oceanography, and International Pacific Research Center, University of Hawaii at Manoa, Honolulu, Hawaii

Patrick F. Cummins

Institute of Ocean Sciences, Fisheries and Oceans Canada, Sidney, British Columbia, Canada

ABSTRACT

An ocean model is used to examine and compare the forcing mechanisms and underlying ocean dynamics of two dominant modes of ocean variability in the northeast Pacific (NEP). The first mode is identified with the Pacific decadal oscillation (PDO) and accounts for the most variance in model sea surface temperatures (SSTs) and sea surface heights (SSHs). It is characterized by a monopole structure with a strong coherent signature along the coast. The second mode of variability is termed the North Pacific Gyre Oscillation (NPGO). This mode accounts for the most variance in sea surface salinities (SSSs) in the model and in long-term observations. While the NPGO is related to the second EOF of the North Pacific SST anomalies (the Victoria mode), it is defined here in terms of SSH anomalies. The NPGO is characterized by a pronounced dipole structure corresponding to variations in the strengths of the eastern and central branches of the subpolar and subtropical gyres in the North Pacific. It is found that the PDO and NPGO modes are each tied to a specific atmospheric forcing pattern. The PDO is related to the overlying Aleutian low, while the NPGO is forced by the North Pacific Oscillation. The above-mentioned climate modes captured in the model hindcast are reflected in satellite altimeter data.

A budget reconstruction is used to study how the atmospheric forcing drives the SST and SSH anomalies. Results show that the basinwide SST and SSS anomaly patterns associated with each mode are shaped primarily by anomalous horizontal advection of mean surface temperature and salinity gradients ($\nabla \bar{T}$ and $\nabla \bar{S}$) via anomalous surface Ekman currents. This suggests a direct link of these modes with atmospheric forcing and the mean ocean circulation. Smaller-scale patterns in various locations along the coast and in the Gulf of Alaska are, however, not resolved with the budget reconstructions. Vertical profiles of the PDO and NPGO indicate that the modes are strongest mainly in the upper ocean down to 250 m. The shallowness of the modes, the depth of the mean mixed layer, and wintertime temperature profile inversions contribute to the sensitivity of the budget analysis in the regions of reduced reconstruction skill.

1. Introduction

Understanding large-scale climate variations is crucial for improving large-scale and regional climate predictability, as well as for being able to discern the anthropogenic influence on climate variability. One of the most documented modes of large-scale climate variability over the North Pacific is characterized by the leading principal component of North Pacific monthly sea surface temperatures anomalies (SSTAs), which varies on interannual and decadal time scales, and is known as the Pacific decadal oscillation (PDO) index (Davis 1976; Mantua et al. 1997). The PDO, also evident in sea surface heights (SSHs), has been linked to the 1976–77 large-scale climate shift over the Pacific (Miller et al. 1994a) during which there were also overlapping changes in the atmosphere, including an intensification

---

Corresponding author address: Emanuele Di Lorenzo, School of Earth and Atmospheric Sciences, Georgia Institute of Technology, 311 Ferst Drive, Atlanta, GA 30332-0340.
E-mail: edl@eas.gatech.edu

of the Aleutian low (Graham 1994; Trenberth and Hurrell 1994). Fluctuations in various oceanic biota have also been shown in several studies to correspond to changes in the sign of the PDO index (Mantua et al. 1997; Hare and Mantua 2000; Chavez et al. 2003; McGowan et al. 2003). As such, ecological and climate variability in the North Pacific have largely been thought to be regulated by the PDO.

Recent studies have suggested that additional modes may significantly influence the climatic variability of the northeast Pacific (NEP). Bond et al. (2003) examined the large SST changes that occurred during the 1999–2002 period and showed that the second mode of North Pacific variability, termed the Victoria mode, contributed importantly to these changes. Recent work by Di Lorenzo et al. (2009, manuscript submitted to *Geophys. Res. Lett.*, hereafter DIL; Di Lorenzo et al. 2008) introduced a new mode of climate variability called the North Pacific Gyre Oscillation (NPGO; information available online at http://www.ocean3d.org/npgo), which emerges from an analysis of sea surface height anomalies (SSHAs) in a model of the NEP. The NPGO, defined as the second leading principal component of NEP SSHAs, is statistically independent from the PDO and is more closely related to the Victoria mode. DIL and Di Lorenzo et al. (2008) showed that the NPGO is significantly correlated with decadal variations of salinity and key biological parameters including chlorophyll-a and NO_3 throughout the NEP, indicating that this mode also has a strong impact on physical and biological conditions in the North Pacific Ocean. The NPGO is part of a global climate pattern that has been observed to strengthen in the last decade or so (DIL; Di Lorenzo et al. 2008) and corresponds to a strengthening of the Victoria mode over this period. As discussed below, the NPGO is the oceanic expression of the so-called North Pacific Oscillation (NPO), an atmospheric pattern first described by Walker and Bliss (1932).

In this paper, we show how the NPGO together with the PDO contributes to a more complete characterization of NEP climate variability. Given that the NPGO has not received as much attention as the PDO, this paper explores the characteristics and underlying dynamics of the NPGO in detail and how these compare to those of the PDO. In particular, we seek to isolate the underlying physical processes that force the NPGO and examine how these are distinguished from those that drive the PDO. The PDO has been shown to be controlled by a combination of changes in surface heat fluxes and horizontal advection anomalies, related to anomalies of the overlying atmosphere (i.e., the Aleutian low; Miller et al. 1994a). As for the NPGO, Di Lorenzo et al. (2008) found that it correlates well

with alongshore wind stress along the coast, but did not explore the physical mechanisms that may contribute to the entire large-scale structure of the mode in the North Pacific. A number of previous studies have shown that atmospheric forcing is important in driving low-frequency SSH and upper-layer thickness variability over the NEP (Lagerloef 1995; Cummins and Lagerloef 2004; Capotondi et al. 2005). Here we present a detailed analysis of the ocean surface temperature and salinity budgets in order to elucidate how atmospheric forcing drives the low-frequency oceanic variability reflected both in the NPGO and PDO.

Use is made of an ocean model hindcast to analyze the two above-mentioned modes of decadal variability. We restrict most of our analysis to the region of the NEP because of the potentially large impact both modes have in this region, especially along the North American coastline. Though as noted in Di Lorenzo et al. (2008), the global pattern of the NPGO suggests decadal variability across the entire Pacific Ocean that may have implications for many regions throughout the Pacific basin.

The structure of this paper is as follows. Section 2 is an overview of the ocean model configuration and forcing functions; section 3 describes the NPGO and PDO from the model hindcast and includes a comparison of the low-frequency response of the model with satellite data as well as an analysis linking the PDO and NPGO to atmospheric forcing patterns. Section 4 describes the surface temperature and salinity budget reconstructions for each mode. In section 5 we use the budget reconstructions to describe how the spatial patterns of each mode are shaped relative to one another. The vertical expression of each mode is described in section 6, and a summary and discussion follows in section 7. Companion work to this paper will include a detailed regional analysis of the impact of these different climate regimes on eastern boundary currents as well as a detailed analysis of how the NPGO is reflected in various observational datasets. Both will be reported elsewhere.

2. Model configuration and validation

The ocean model experiments in this study were conducted with the Regional Ocean Modeling System (ROMS), a free-surface, hydrostatic, primitive-equation ocean model with terrain-following coordinates in the vertical and generalized orthogonal curvilinear coordinates in the horizontal (Haidvogel et al. 2000; Shchepetkin and McWilliams 2004; Haidvogel et al. 2008). ROMS uses a split-explicit time-stepping scheme to solve the hydrostatic primitive equations of momentum where there is special coupling between barotropic (fast) and baroclinic (slow) modes (Shchepetkin and McWilliams

2004). ROMS has provided reliable results for other regional and basinwide studies of the North Pacific Ocean (Di Lorenzo 2003; Marchesiello et al. 2003; Capet et al. 2004; Curchitser et al. 2005; Di Lorenzo et al. 2005; Moore et al. 2009).

In this study, ROMS is configured for the NEP, the domain covering 25°–61°N, 179°–111°W. This domain encompasses the Gulf of Alaska (GOA), the California Current System (CCS), and portions of the North Pacific subpolar and subtropical gyres. The average horizontal resolution is 15 km and there are 30 terrain-following s levels in the vertical. Model initial conditions were obtained from Levitus et al. (1994) data. At the three open boundaries, a modified radiation condition (Marchesiello et al. 2003) is used together with nudging to Levitus et al. (1994) climatologies. We performed an ocean model hindcast (1950–2004) with ROMS using as surface forcing monthly mean wind stress from the National Centers for Environmental Prediction (NCEP), a combination of climatological heat fluxes and nudging to observed SST, and climatological freshwater fluxes. Monthly climatologies for heat and freshwater fluxes are computed from an 80-yr spinup integration that uses nudging to climatological sea surface temperature (SST) and sea surface salinity (SSS). For heat fluxes we add a nudging factor that relaxes the model SSTs toward time-dependent (1950–2004) monthly mean SSTs from the National Oceanic and Atmospheric Administration (NOAA; Smith and Reynolds 2004). The time scale of the nudging is approximately 30 days and its contribution to the net heat flux does not seem to play an important role in the dynamics that shape the spatial structure of the SST and SSS anomalies associated with PDO and NPGO (see section 4). The above-mentioned model integration is the same as that in Di Lorenzo et al. (2008) and DIL and captures observed fluctuations in temperature, salinity, and nutrients observed in the California Current [California Cooperative Oceanic Fisheries Investigations (CalCOFI)] and Gulf of Alaska (Line P). An analysis of the ROMS hindcast follows.

3. Modes of decadal variability

a. Properties of the PDO and NPGO

By performing an empirical orthogonal function (EOF) analysis of the output from the model hindcast, we are able to isolate the PDO and NPGO modes of variability. We define the model PDO index as the first principal component (PC1) of model SSHAs; it closely tracks the observed PDO index (Mantua et al. 1997) as seen in Fig. 1a. By regressing the model PDO index with the model SSHAs (Fig. 1c), we see that a positive PDO

in the model is associated with higher SSHs along the entire North American coast and lower SSHs offshore and in the central part of the domain, which reflects a weakening of the subtropical gyre and coastal California Current and a strengthening of the Alaskan Gyre and, hence, the coastal Alaskan Current. We define the model NPGO index as PC2 of the model SSHAs (Fig. 1b). The regression of the model NPGO index with the model SSHA shows a clear dipole pattern corresponding to the intensification of the central and eastern branches of the subtropical and subpolar gyre of the North Pacific (Fig. 1d). During a positive NPGO in the model, both gyres intensify, thus increasing the strength of the northward coastal Alaskan Current and the southward coastal California Current. For both modes, the SSHA pattern corresponds to Ekman pumping anomalies (contour lines, Figs. 1c,d) indicating that the modes are driven by variations in wind stress curl. We shall investigate this link with atmospheric forcing in section 3c.

The model PDO index closely tracks PC1 of the model SSTAs, and likewise the model NPGO index closely tracks PC2 of the model SSTAs (Di Lorenzo et al. 2008). The spatial structures of SSTAs for each mode are found by regressing the indices to the model SSTAs. This yields patterns that are similar to the above-mentioned SSHA patterns with a coherent signal along the North American coast associated with the model PDO index and a dipole structure associated with the model NPGO index (Figs. 1e,f). For both the PDO and NPGO patterns, the strongest SSTAs are generally located in regions where the anomalous surface Ekman currents (black arrows, Figs. 1e,f) are normal to the mean SST gradients (contours, Figs. 1e,f). However, we will show in the next section that other physical processes also contribute to the underlying dynamics of these modes. The patterns of SSHAs and SSTAs associated with the PDO explain the most variance in the model SSH (22%) and SST (34%), while the same patterns associated with the NPGO account for 8% and 21% of the variance, respectively.

Though the model PDO index closely tracks PC1 of the model SSTAs, it does *not* closely track PC1 of the model sea surface salinity anomalies (SSSAs), but rather it is highly correlated[1] with PC2 of the model

---

[1] Note that the correlations in this paper are all >95% significant and were estimated from the probability distribution functions (PDFs) of the correlation coefficient of two red noise time series that possessed the same lag-1 autoregression coefficients as the original signals. The PDFs were computed numerically by generating 1000 realizations of the correlation coefficient of two random red noise time series following Di Lorenzo et al. (2008).
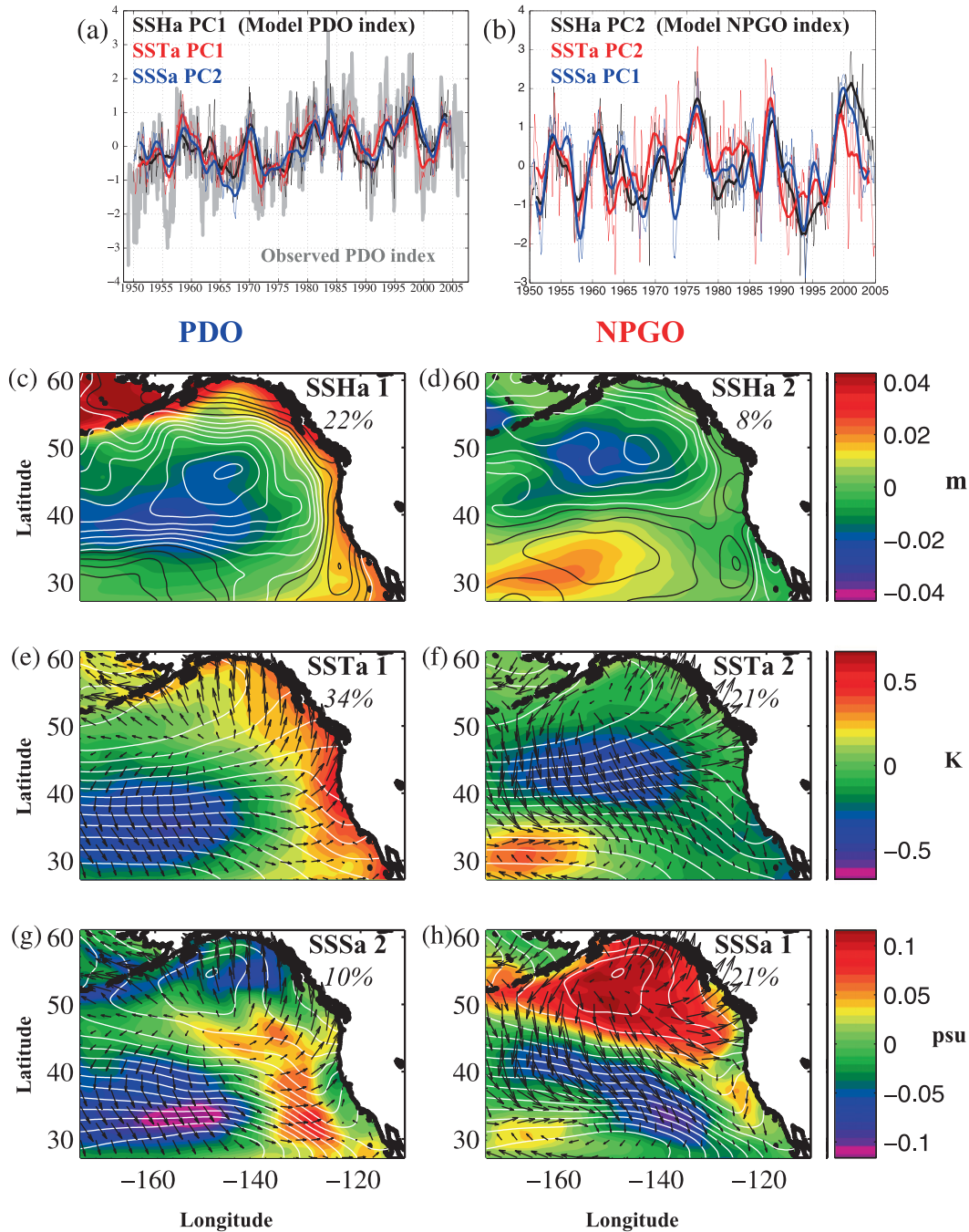
FIG. 1. (a) Time series of the observed PDO index (gray line) and PC1 of SSHA (i.e., the model PDO index) (black line), PC1 of SSTA (red line), and PC2 of SSSA (blue line) of the ocean model hindcast. All time series are plotted in standard deviation units with the 2-yr low-passed time series plotted in bold. (b) Time series of PC2 of SSHA (i.e., the model NPGO index; black line), PC2 of SSTA (red line), and PC1 of SSSA (blue line). Regression maps of the model (c) PDO and (d) NPGO index, respectively, with the model SSHA. White (black) contours correspond to regions of positive (negative) Ekman pumping and are based on a regression of the model PDO and NPGO index with the NCEP wind stress curl. (e)–(h) Black arrows correspond to wind-driven Ekman currents based on a regression of the model PDO and NPGO index with the model ocean currents. Regression maps of the model (e) PDO and (f) NPGO index with the model SSTA. White contours correspond to the climatological mean SST gradients with cooler SSTs in the GOA. Regression maps of the model (g) PDO and (h) NPGO index with the model SSSA. White contours correspond to the climatological mean SSS gradients with fresher waters in the GOA. The percentage explained variance by each regression map is denoted in (a)–(h).

SSSAs ($r = 0.65$). Additionally, the model NPGO index is more highly correlated with PC1 of SSSAs ($r = 0.67$) than with PC2 of SSSAs ($r = 0.07$). As such, the PDO accounts for less of the total variance in model SSS (10%; see Fig. 1g) than the NPGO (21%; see Fig. 1h). The SSSA patterns associated with each mode are quite different from the respective spatial patterns of SSHAs and SSTAs. During a positive phase of the PDO, there is considerable spatial inhomogeniety in the SSSAs, especially along the coastline (Fig. 1g). During a positive phase of the NPGO, SSSAs are highest in the northern part of the domain, particularly in the GOA and, as with the PDO, there is spatial inhomogeniety along the coastline. Note that the SSSA associated with the NPGO is dominated by a large-scale coherent pattern that has not been described before. As with the SSTAs, strong SSSAs appear in regions where the anomalous wind driven currents are aligned normal to the mean SSS gradients (contours, Figs. 1g,h), with exceptions along the coast *and* in the GOA where surface currents (black arrows, Figs. 1g,h) are less coherent. In subsequent sections, we will show that in these regions, Ekman pumping influences the characteristics of these modes.

The total spatial variance of these modes does not imply that, locally, these modes explain a lot more variance. However, the above-mentioned anomaly patterns clearly differ between the PDO and NPGO, indicating that specific regions may be "dominated" by a particular mode. Figure 2 shows the difference in the magnitude of the anomaly patterns (SSHA in Fig. 2a, SSTA in Fig. 2b, and SSHA in Fig. 2c) between the two climate modes where regions of negative values (black contours) indicate that the NPGO dominates and regions of positive values (white contours) indicate that the PDO dominates. It is not surprising that the SSHA and SSTA along the coastline are primarily influenced by the PDO, while in the interior of the basin, the NPGO and PDO dominate different areas. With respect to SSSAs, however, the NPGO is the more dominant mode, especially along the coast, because of the strong SSSA monopole in the GOA and a stronger coastal signal that characterizes the NPGO. Note that the coastal signal of the NPGO SSSA is not uniform, and hence between 40° and 50°N, the PDO dominates. Like with SSHAs and SSTAs, the NPGO and PDO influence SSSAs in different areas of the interior away from the coast.

b. Comparison with satellite observations

The large-scale, low-frequency response of the model is assessed by comparing the last 12 yr of the model simulation (1993–2004) to SSHA observations for the same time period from the Ocean Topography Experiment (TOPEX)/Poseidon (T/P) altimeter. To this end, a
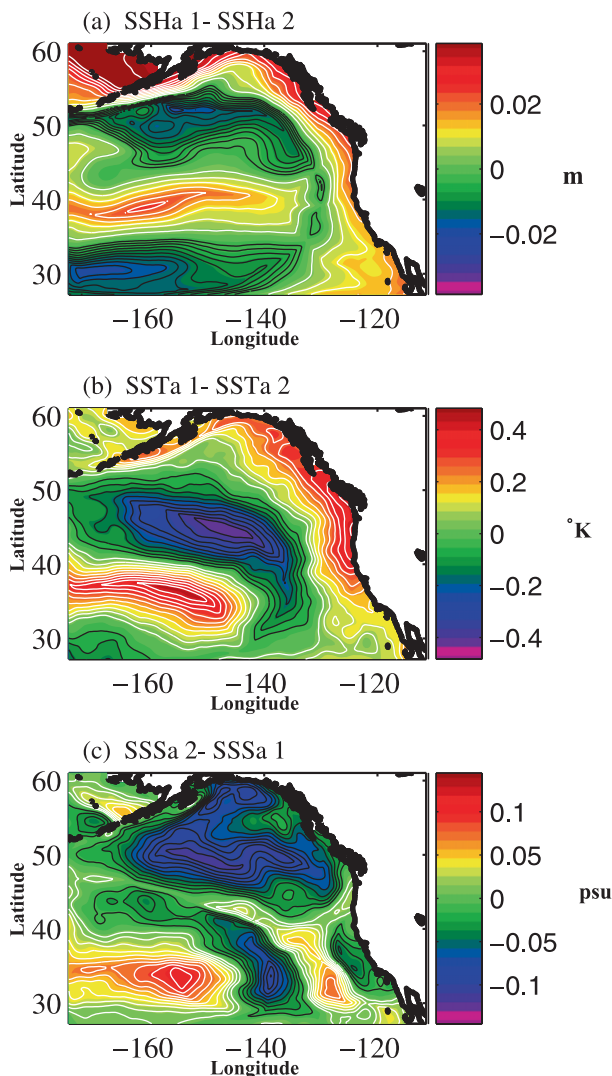

FIG. 2. The difference between PDO and NPGO regression maps of (a) SSHA, (b) SST, and (c) SSS. White contour lines denote where the PDO dominates while black contour lines denote where the NPGO dominates.

canonical correlation analysis (CCA) was used to relate the leading EOFs of the T/P observations to the leading modes of the model SSHAs (Barnett and Preisendorfer 1987). The EOFs of observed SSHA over the NEP were computed from the T/P data gridded at $1° \times 1°$ resolution. Note that prior to computation of these modes, monthly means were removed from the data and a 3-month boxcar filter was applied to the residual to suppress short-term variability. The EOFs of the model SSHAs were computed in a similar way, with the model fields subsampled at every third point in each direction to reduce the computational effort and maintain comparable resolution with the T/P data. We found that using either three or four EOFs as inputs to the CCA
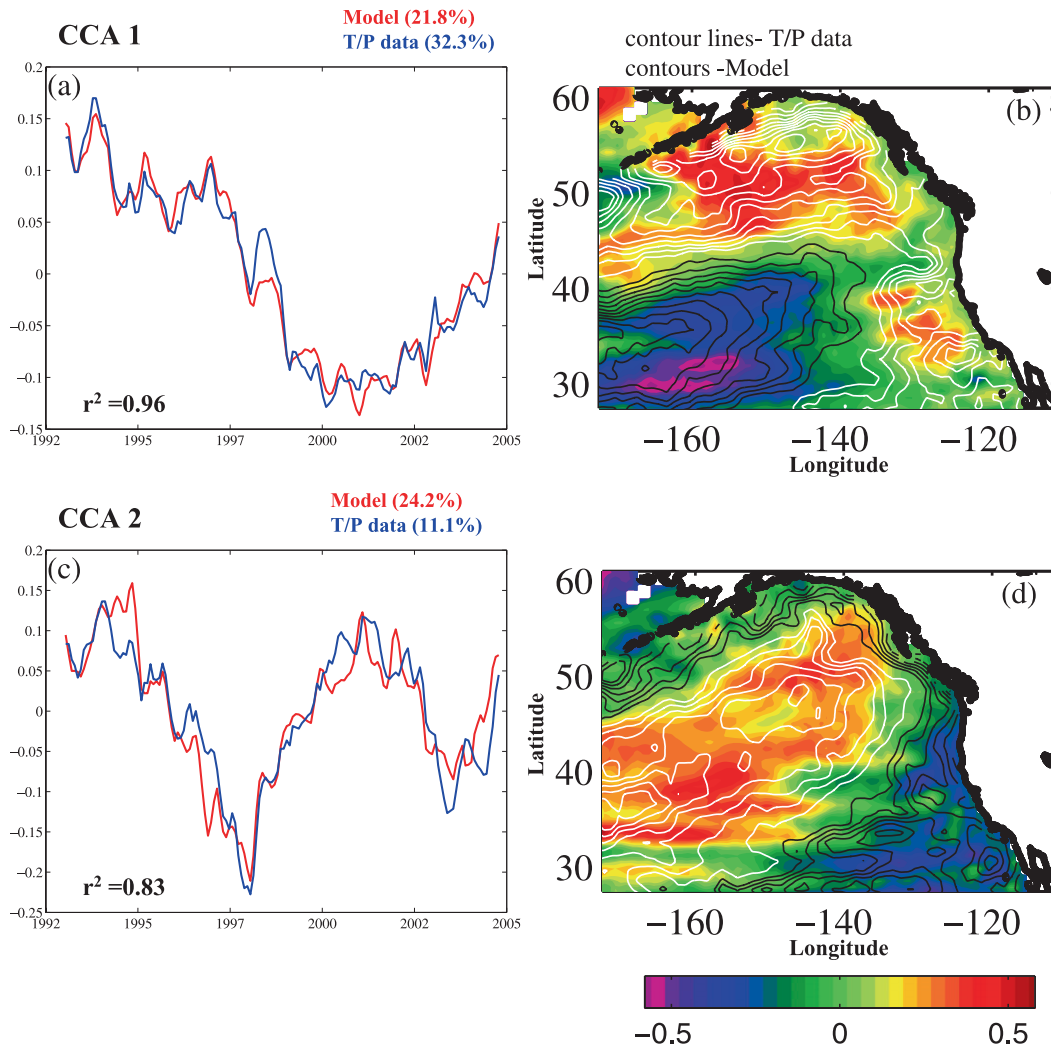
FIG. 3. (a),(c) Amplitude time series and (b),(d) spatial patterns from a canonical correlation analysis of T/P satellite altimeter data and the model SSHA for the 12-yr period, 1993–2004 (see section 3b). The amplitude time series for the model (data) are plotted in red (blue). Color contours are used to depict spatial patterns for the model, while contour lines are used for the data fields with white (black) lines for positive (negative) contours.

gave optimal results. As such, the following discussion is based on using the three leading EOFs from the model and from the T/P data as inputs to the CCA.

The amplitude time series and spatial patterns of the first canonical mode (CCA1) and the second canonical mode (CCA2) are shown in Figs. 3a,c and 3b,d, respectively. Together, these two CCA modes account for a similar fraction of the interannual variability of the model (46%) and of the observations (43.4%), although CCA1 (CCA2) is relatively less (more) important in the model than in the observations. The amplitude time series of the model and data are closely related to each other, with strong canonical correlations for both CCA1 ($r^2 = 0.96$) and CCA2 ($r^2 = 0.83$). The spatial fields (Figs. 3b,d) pertaining to these modes also show a

general agreement, indicating that the amplitude time series for the model and data share similar spatial patterns over the northeast Pacific. Overall, the close agreement between model and observations found in the leading canonical modes provides some confidence that the model accurately represents the large-scale low-frequency variability over this region.

It is evident from inspection of the amplitude time series and the structure of the spatial patterns that CCA1 corresponds approximately to the NPGO mode, while CCA2 resembles the PDO mode. CCA1 describes a regime-like change following the La Niña event of 1999 and lasting through 2003, which coincides with a strengthening of the NPGO in SSTAs and SSHAs after 1990. This La Niña event consisted of a broad region of

rising sea level over the central Pacific, accompanied by a lowering of sea level in the Gulf of Alaska and off the west coast of North America (Cummins et al. 2005). The spatial patterns of CCA2 (Fig. 3d), particularly for the T/P data (black and white contours), include contours that broadly follow the coastline, spanning the subtropical and subpolar gyres, and are associated with anomalous geostrophic flow along the coast. This mode reaches maximum intensity in early 1998 as the SSH signal associated with the 1997/98 El Niño reached its maximum over extratropical latitudes along the west coast of North America (Strub and James 2002). There is a second smaller peak in 2003, apparently associated with the relatively weak El Nino of 2002/03.

c. Atmospheric forcing of the PDO and NPGO

Numerous studies have shown that the PDO is linked to anomalous changes in overlying atmospheric sea level pressure (SLP) patterns (Latif and Barnett 1994; Zhang 1996; Zhang et al. 1997; Hare and Mantua 2000), in particular the Aleutian low, which has been observed to weaken during a negative phase of the PDO (Bond et al. 2003) and strengthen during a positive phase (Graham 1994). To date, the NPGO has not been linked to any such atmospheric forcing pattern. Here we explore the extent to which the two modes are atmospherically forced. To this end, the atmospheric forcing patterns associated with the PDO and NPGO are isolated by regressing global NCEP sea level pressures anomalies (SLPAs) with the model PDO and NPGO indices. The monopole structure of SLPa associated with the PDO (Fig. 4a) is consistent with the structure and expanse of the Aleutian low (Rodionov et al. 2005). The dipole structure associated with the NPGO (Fig. 4c), on the other hand, is consistent with the so-called North Pacific Oscillation (NPO) in which there is direct opposition in SLP variations over Hawaii and Alaska (Walker and Bliss 1932). Note that the SLPAs associated with each mode are both consistent with wind stress data from NCEP (black arrows, Figs. 4a,c).

To quantify the response to atmospheric forcing, we use a simple model for each modal index, similar to Schneider and Cornuelle (2005) and Newman et al. (2003). The modal indices in this simple model, denoted by I, are governed by an autoregressive (AR)-1 process forced by a prescribed forcing index, denoted f_t, and can be written as

$$I_t = \alpha I_{t-1} + \beta f_t + \eta_t. \tag{1}$$

Equation (1) is initialized with either the model NPGO index or the model PDO index at the beginning of year 1950. The coefficients α and β are obtained by a least squares estimation and η_t is uncorrelated noise. To re-

construct the PDO index, we define f_t as the SLPA averaged over the NEP (red box shown in Fig. 4a). The reconstructed PDO index found from (1) and the above-mentioned f_t correlates at 0.56 with our model PDO index (i.e., PC1 of model SSHA) as seen in Fig. 4b. Note that our prescribed forcing f_t is similar ($r = 0.8$) to the North Pacific (NP) index defined as PC1 of SLP in the North Pacific, which yields a similar PDO index reconstruction (green line, Fig. 4b). Our results are also consistent with Schneider and Cornuelle (2005), who found that SLPA in the North Pacific had high skill in reconstructing the observed PDO amplitude.

To reconstruct the NPGO index, we define f_t as the difference between SLPA averaged over a portion of the subpolar gyre region (top red box denoted in Fig. 4c) and SLPA averaged over a portion of the subtropical gyre region (bottom red box denoted in Fig. 4c). As mentioned above, this forcing index is consistent with the NPO (Walker and Bliss 1932) and we find it has skill in reconstructing the NPGO index (Fig. 4d). The reconstructed NPGO index obtained from (1) and the model NPGO index (i.e., PC2 of model SSHA) are correlated at 0.71 (Fig. 4d), suggesting that, like the PDO, the NPGO climate signature likely occurs as an integrated response to atmospheric forcing.[2] As with the PDO, f_t associated with the NPGO coincides ($r = 0.89$) with the NPO index defined as PC2 of SLP in the North Pacific, which yields a similar NPGO index reconstruction (green line, Fig. 4d). This is consistent with Cummins and Lagerloef (2004), who found that a Markov model driven by Ekman pumping reproduced the leading mode of SSHAs over the NEP. Thus, the NPGO appears as the oceanic expression of the NPO (Walker and Bliss 1932). The coefficient α from these reconstructions indicates that the damping time scale of the NPGO is about 2 times longer than that of the PDO, which has a damping time scale of about 5.5 months, suggesting that the NPGO has more low-frequency power.

4. Budget analysis

Based on the model hindcast, the variances in model SST are dominated by the PDO, while the NPGO controls

---

[2] The statistical significance of the AR1 reconstruction of the PDO and NPGO index was tested using a Monte Carlo simulation; 1500 realizations of f_t associated with the PDO and NPGO were generated using the same periodogram as the original forcing f_t, but with random phases. These realizations were used as input to the AR1 model in (1) and the correlation of each realization with the model PDO and NPGO index was computed. The PDF of these 1500 correlations reveal that the AR1 reconstructions from the original prescribed forcings f_t for the PDO and the NPGO are 99% significant.
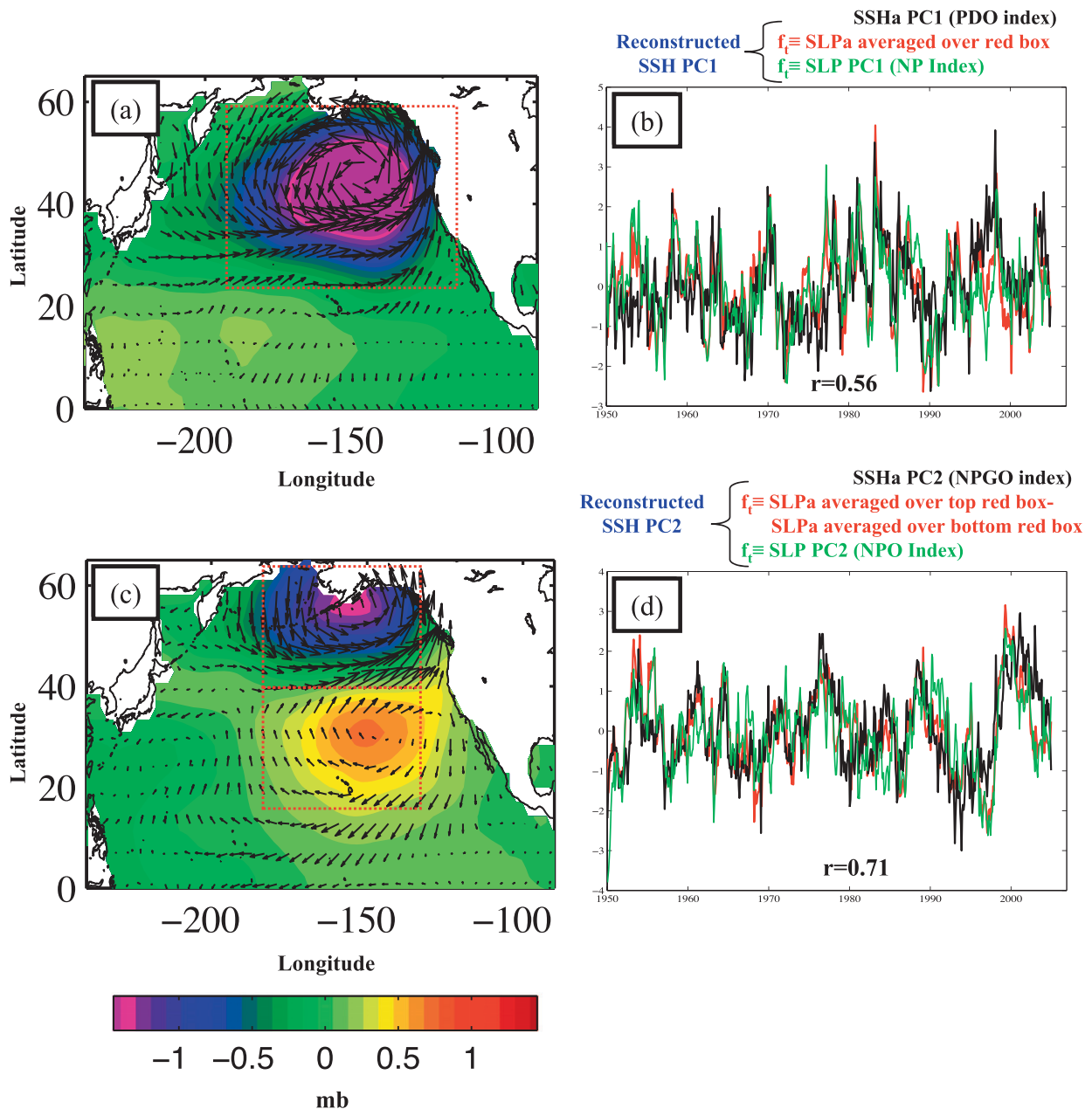
FIG. 4. Regression maps of the model (a) PDO index and (c) NPGO index with North Pacific NCEP SLPA illustrating the spatial patterns of atmospheric forcing associated with each mode. Black arrows correspond to wind stress vectors based on a regression of the model PDO and NPGO index with NCEP wind stress. Also shown are the time series of the model (b) PDO and (d) NPGO index in black and (b) PDO and (d) NPGO index reconstructions from an AR-1 process forced by some prescribed forcing f_t. The red lines are reconstructions from f_t that are defined as the SLPA averaged over the NEP [red box in (a) for the PDO and the difference between the SLPA averaged over the top red box in (b) and the SLPA averaged over the bottom red box in (b) for the NPGO]. The green lines are reconstructions from f_t that is defined as PC1 (NP index) and PC2 (NPO index) of North Pacific SLP.

more of the model variance in SSS. To support this, Di Lorenzo et al. (2008; DIL) showed that the model PDO index and NPGO index, respectively, agree with SST and SSS variations in the CCS recorded by the CalCOFI and Line P (Crawford et al. 2007). Additionally, it was

shown that the model NPGO index agrees well with observed key biological nutrients such as chlorophyll-a (Chla) and subsurface NO_3 from CalCOFI and with alongshore wind stress from NCEP. As such, it is important to understand the atmospherically driven ocean

dynamics of each of these climate modes because they both potentially have a strong impact on North Pacific climate and the physical and ecological condition of the NEP.

To determine how atmospheric forcing influences the ocean dynamics of each mode, we examined the different physical processes that contribute to the anomalous surface temperature and salinity budgets associated with each mode. The following AR-1 model (Hasselmann 1976) is considered for SST anomalies T' and SSS anomalies S':

$$\frac{\partial T'}{\partial t} \cong -\alpha T'$$
$$+ \left(-\mathbf{u}' \cdot \nabla \overline{T} - \overline{\mathbf{u}} \cdot T' - \overline{w_E} \frac{dT'}{dz} - w_E' \frac{d\overline{T}}{dz} - \frac{q'}{\rho_0 C_p \overline{H}} \right),$$

(2)

$$\frac{\partial S'}{\partial t} \cong -\alpha S' + \left(-\mathbf{u}' \cdot \nabla \overline{S} - \overline{\mathbf{u}} \cdot S' - \overline{w_E} \frac{dS'}{dz} - w_E' \frac{d\overline{S}}{dz} \right),$$

(3)

where α is the damping rate as in (1), the $\mathbf{u}$ are the horizontal Ekman current vectors, w_E is the Ekman pumping that does not include the coastal upwelling component, and dT/dz and dS/dz are the maximum vertical gradients of temperature and salinity within the mixed layer depth H, which is taken as the depth at which the gradient of density is largest. Net surface heat fluxes are represented by q, $\rho_0 = 1025$ kg m^{-3} is the mean density of seawater, and $C_p = 3986$ J kg^{-1} K^{-1} is the heat capacity of seawater. The variables in (2) and (3) with an overbar (i.e., $\overline{S}$) represent climatological means, and variables with a prime (i.e., S') represent anomalies. Note that the terms on the right-hand side (rhs) of (2) and (3) enclosed in parenthesis represent linearized forcing terms. If we regress either the PDO or NPGO index, denoted by I, with (2) and (3) and assume that month-to-month variations of SST and SSS anomalies are small, we have

$$T_I' \cong$$
$$\left(-\mathbf{u}_I' \cdot \nabla \overline{T} - \overline{\mathbf{u}} \cdot \nabla T_I' - \overline{w_{E_I}} \frac{dT_I'}{dz} - w_{E_I}' \frac{d\overline{T}}{dz} - \frac{q_I'}{\rho_0 C_p \overline{H}} \right) / \alpha,$$

(4)

$$S_I' \cong \left(-\mathbf{u}_I' \cdot \nabla \overline{S} - \overline{\mathbf{u}} \cdot \nabla S_I' - \overline{w_{E_I}} \frac{dS_I'}{dz} - w_{E_I}' \frac{d\overline{S}}{dz} \right) / \alpha, \quad (5)$$

where, for simplicity, we have denoted anomalies that have been regressed with a climate index by a subscript

I. Equations (4) and (5) show that the anomalous surface temperature and salinity budgets associated with the PDO and the NPGO (i.e., $I \equiv$ PDO, $I \equiv$ NPGO) are controlled by several different physical processes. These physical processes are (a) anomalous horizontal advection of mean SST and SSS [first terms on rhs of (4) and (5)], (b) mean horizontal advection of SSTAs and SSSAs [second terms on rhs of (4) and (5)], (c) mean vertical advection of anomalous temperature and salinity [third terms on rhs of (4) and (5)], (d) and anomalous vertical advection of mean temperature and salinity [fourth terms on rhs of (4) and (5)] via Ekman pumping, and (e) net surface heat fluxes acting on the mean mixed layer [last term on rhs of (4)]. Based on the damping time scales found in the previous section, $1/\alpha = 2.5$ months for the PDO and $1/\alpha = 5$ months for the NPGO, and these give the best reconstruction of the SSTAs and SSSAs associated with each mode.

If (4) and (5) are good representations of the model SSTA and SSSA budgets, the sum of terms on the rhs of (4) and (5) (i.e., T_I' and S_I') should resemble the SSTA and SSSA patterns in Figs. 1e–h. As such, by computing each of the physical processes in the anomalous surface temperature and salinity balances in (4) and (5), the physical mechanisms that are important for driving the underlying dynamics of each mode may be identified.

In the following sections, we will show that the computed anomalous horizontal advection and Ekman pumping terms in (4) and (5) consistently reconstruct the basinwide, large-scale SSTA and SSSA patterns associated with the PDO and NPGO fairly well, although the reconstruction of smaller-scale variations in the GOA and in various places along the coast is not always as skillful. This suggests that we may not be able to reliably assess the dynamics that drive the modes in small, localized areas to the same extent that this is possible for the interior of the basin. We will address this issue later in section 6. Note that, although our definition of the vertical gradients in (4) and (5) preclude a seasonal cycle, a series of sensitivity tests (not shown) indicate that the large-scale basinwide reconstruction patterns presented in the following sections are robust to any seasonal stratification.

a. SST budget

The sum of terms on the rhs of (4) for the PDO T'_{PDO} is shown in Fig. 5b, while the actual SSTAs associated with the PDO are shown in Fig. 5a (same as Fig. 1e). As noted above, we find that it is possible to reconstruct the PDO SSTAs fairly well using the anomalous surface temperature budget described by (4), except in the northern GOA. The pattern correlation between the anomalies from the reconstructed budget and the PDO
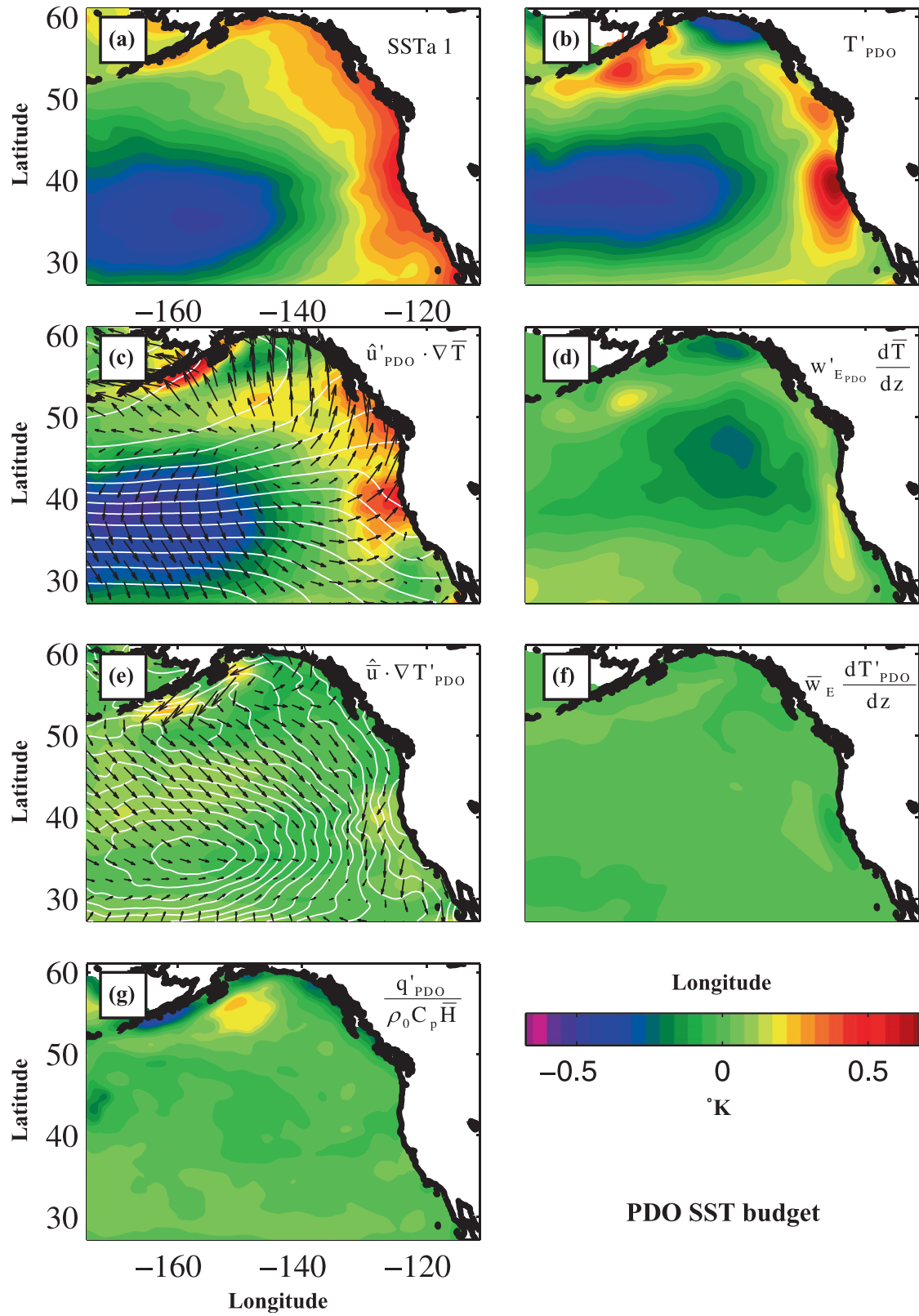
regression map is 0.76 (>99% significant). The strong positive SSTAs along the coast and the strong negative SSTAs offshore in the central part of the domain and in the subtropics (Fig. 5a) are largely driven by anomalous horizontal advection of mean SSTs (Fig. 5c); this is due to the component of anomalous surface Ekman currents (black arrows) oriented normal to the gradient of mean SSTs (white contours), as mentioned previously. Anomalous vertical advection of mean SSTs (Fig. 5d) by Ekman pumping and mean horizontal advection of SSTAs (Fig. 5e) contribute, to a lesser extent, to positive SSTAs in various places along the coast, while the contribution of mean vertical advection (Fig. 5f) to SSTAs by Ekman pumping is relatively small throughout the basin. Heating via net surface heat fluxes (Fig. 5g) tends to be largest in the western GOA, contributing to positive SSTAs in this region. The cooling in the GOA that is in our reconstructed T'_{PDO} and *not* in the SSTAs associated with the PDO appears to result from the combination of anomalous horizontal advection and Ekman pumping. While heat fluxes have been shown to be important during the PDO-related climate shift and on longer time scales (Miller et al. 1994b; Dawe and Thompson 2007), they do not seem to play a dominant role in shaping the PDO pattern.

As with the PDO, the SSTA pattern associated with the NPGO may be reconstructed from the sum of terms on the rhs of (4). This is shown in Fig. 6b, while the actual SSTA pattern associated with the NPGO is shown in Fig. 6a (same as Fig. 1f). The large-scale NPGO SSTA is reproduced fairly well, although the reconstruction again has less skill in the western GOA where the estimates of temperature vertical gradients are more problematic because of strong seasonal stratification. We also note that the Ekman pumping may be inadequate to account for all of the contributions of anomalous vertical advection in this region (Capotondi et al. 2005). The pattern correlation between the anomalies from the reconstructed budget and the NPGO regression map is 0.55 (>99% significant), which is lower than in the PDO case (0.76). The large-scale SSTA pattern (Fig. 6a) consists of a dipole near the central part of the domain. The large area of cooling in this dipole pattern is largely driven by anomalous horizontal advection of mean SSTs (Fig. 6c), while the area of warming in the subtropical region of this dipole pattern is driven by a combination of anomalous horizontal (Fig. 6c) advection of mean temperatures, anomalous Ekman pumping (Fig. 6d), and anomalous surface heat fluxes (Fig. 6g). Though the reconstruction does not have much skill outside of the region containing the dipole pattern, it does capture the cooling near the coast south of about 40°N. This is driven by a combination of anomalous horizontal (Fig. 6c) temperature advection and anomalous Ekman pumping (Fig. 6d). Strong warming in the northwestern GOA and east of the dipole pattern (Fig. 6b) are primarily due to anomalous Ekman pumping (Fig. 6d) and do not agree with the NPGO SSTA in these regions (Fig. 6a). Additionally, the sum of budget terms slightly overestimates the magnitude of warming and cooling of SST associated with the NPGO.

b. SSS budget

Let us now focus our attention on what drives salinity variations for each of these modes by turning to Eq. (5). The sum of terms on the rhs of (5) for the PDO, S'_{PDO}, are shown in Fig. 7b, while the actual SSSAs associated with the PDO are shown in Fig. 7a (same as Fig. 7g). As with SSTAs, we are able to reconstruct the large-scale SSSA patterns, albeit with some discrepancies in the GOA. The pattern correlation between the anomalies from the reconstructed budget and the PDO regression map is 0.66 (>99% significant). We find that the large-scale SSSA patterns associated with the PDO are driven largely by anomalous horizontal advection of mean SSSs (Fig. 7c), with anomalous vertical advection via Ekman pumping (Fig. 7d) and mean horizontal advection (Fig. 7e) contributing to the freshening along the coast south of 40°N. The strong positive SSSAs in the western GOA found from (5) (Fig. 7b) is at variance with the freshening in this region that is seen in the SSS as associated with the PDO (Fig. 7a). This discrepancy is due to a combination of anomalous horizontal advection of mean salinities (Fig. 7c), and anomalous (Fig. 7d) and mean (Fig. 7f) Ekman pumping.

In section 3, we showed that the SSSA associated with the model NPGO mode (Figs. 1h and 8a) accounts for more of the total variance in model SSSA (21%) than the PDO. During the positive phase of the NPGO, SSSA is characterized by a large-scale coherent pattern with salinification

---

FIG. 5. The regression map of the model PDO index with the (a) model SSTA and (b) sum of the SST budget terms. The pattern correlation between the anomalies from reconstructed budget and the regression map is 0.76 (>99% significant). The SST budget terms for the PDO, including (c) anomalous horizontal advection of mean SST gradients, (d) anomalous vertical temperature advection via wind driven Ekman pumping, (e) mean horizontal advection of anomalous SST gradients, (f) mean vertical advection of temperature anomalies via Ekman pumping, and (g) heating from anomalous net surface heat fluxes. The white contours in (c) and (e) are the mean and anomalous SST gradients, respectively, while the black arrows in (c) and (e) are the mean and anomalous surface currents, respectively.
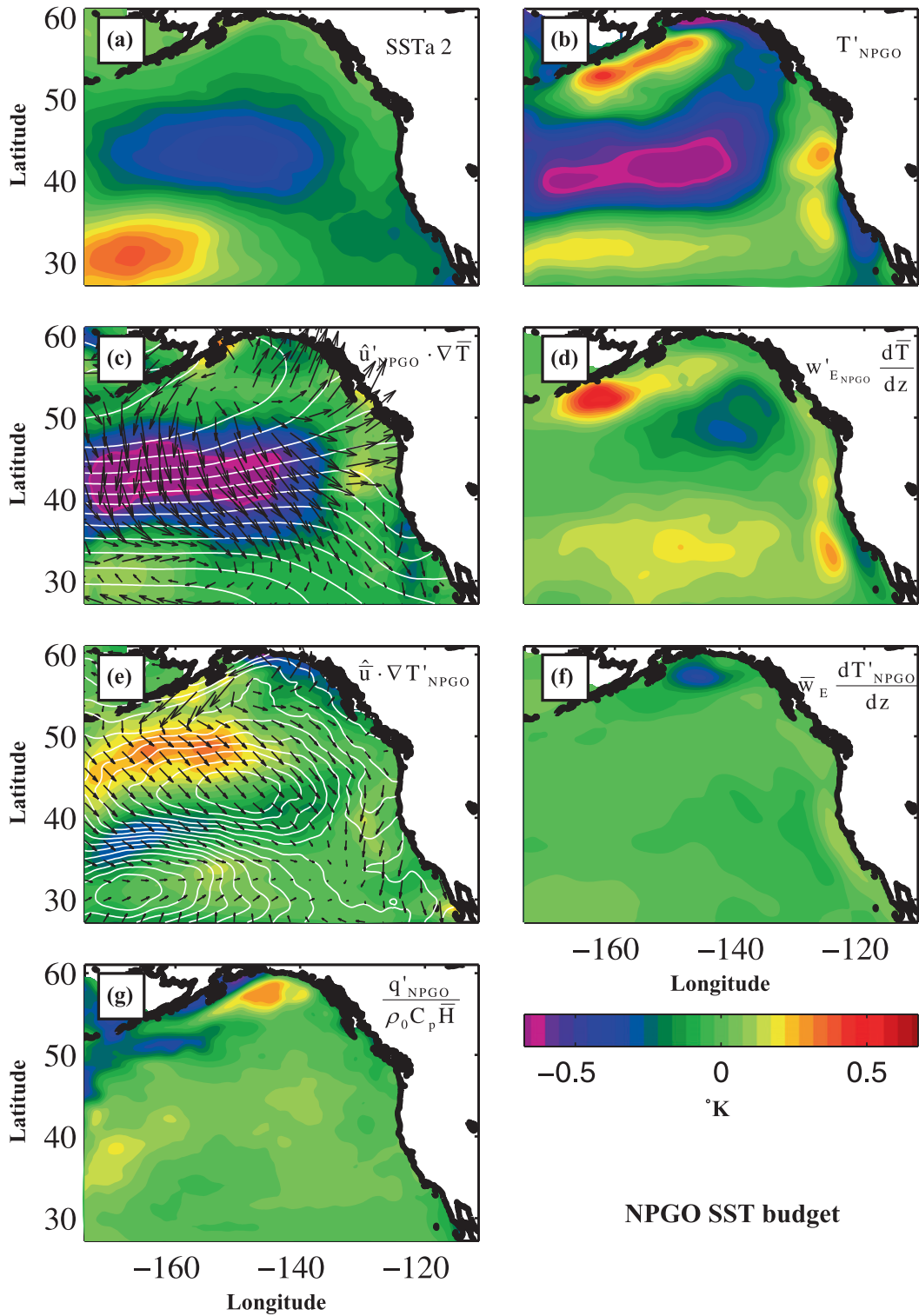
FIG. 6. As in Fig. 5, but for the NPGO. The pattern correlation between the anomalies from the reconstructed budget and the regression map is 0.55 (>99% significant).
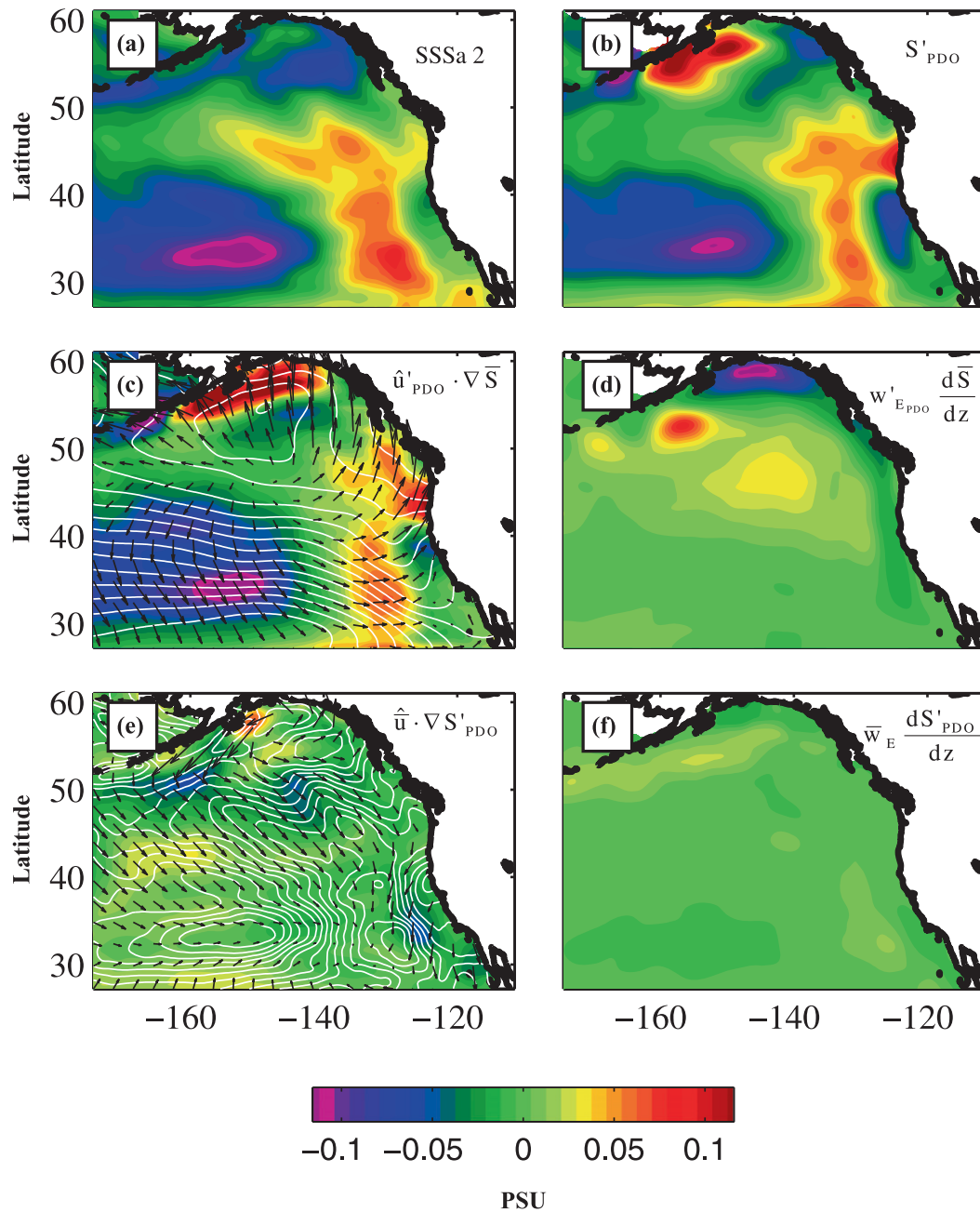
PDO SSS budget

FIG. 7. As in Fig. 5, but for the SSS budget terms. The pattern correlation between the anomalies from the reconstructed budget and the regression map is 0.66 (>99% significant).

throughout the entire GOA and freshening in the northern part of the subtropical gyre. The large-scale structure of this pattern may be reconstructed extremely well from the sum of terms in (5), S'_{NPGO} (Fig. 8b). The pattern correlation between the anomalies from the reconstructed budget and the NPGO regression map is 0.82 (>99%

significant). Thus far we have seen that anomalous horizontal advection of mean gradients appears to be the most influential term on the rhs of (4) and (5) in driving basinwide SSTAs and SSSAs. This is also the case for SSSAs associated with the NPGO as seen in the anomalous horizontal advection of mean SSSs (Fig. 8c). However,
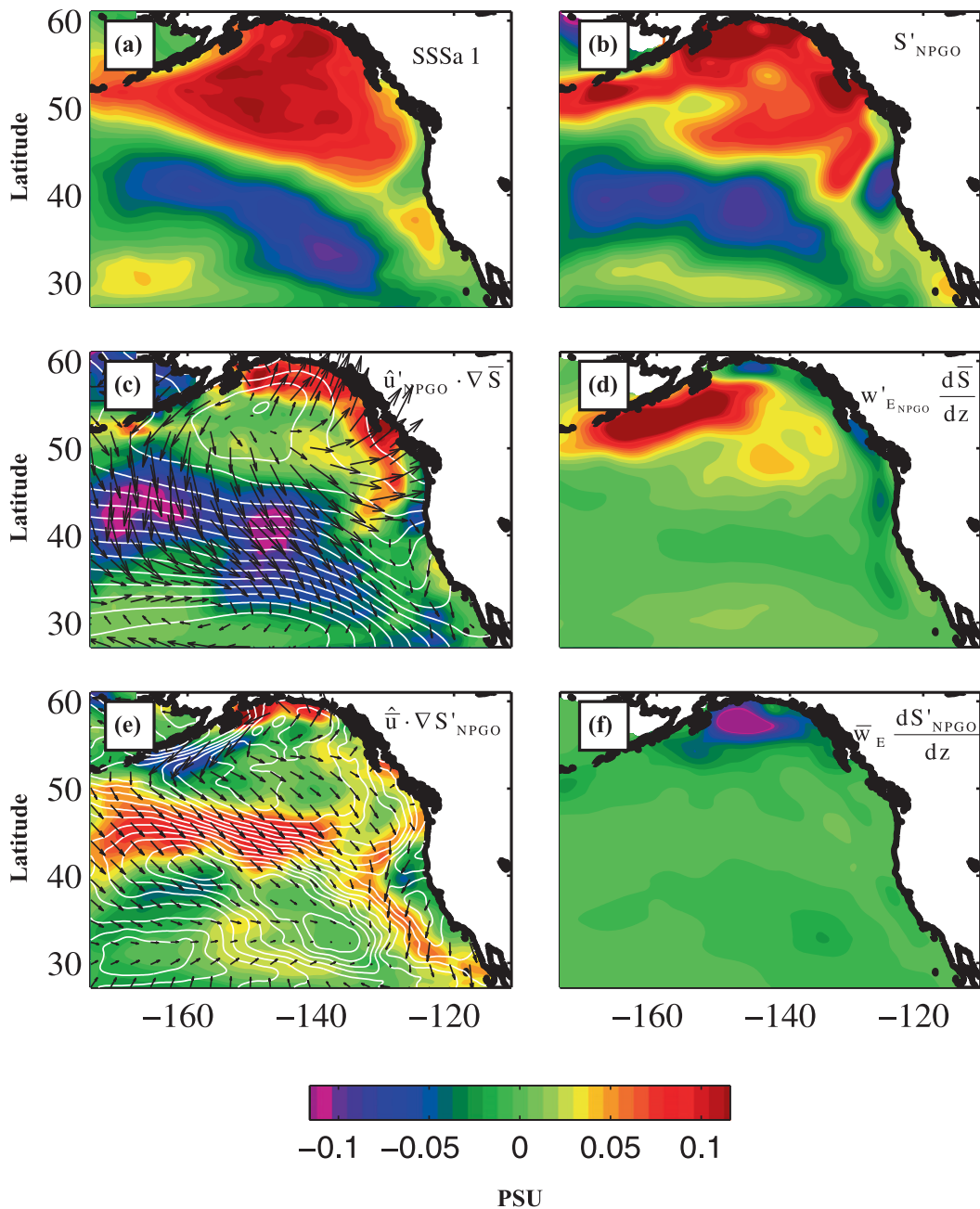
NPGO SSS budget

FIG. 8. As in Fig. 5, but for the NPGO. The pattern correlation between the anomalies from the reconstructed budget and the regression map is 0.82 (>99% significant).

anomalous vertical salinity advection via Ekman pumping (Fig. 8d) and mean horizontal advection of SSSAs (Fig. 8e) are equally important in various parts of the domain and contribute appreciably to the complete picture of the reconstructed NPGO SSSA (Fig. 8b). Anomalous Ekman pumping (Fig. 8d) contributes to strong positive SSSA in

the western GOA. Mean horizontal advection of SSSA (Fig. 8e) contributes to the southern portion of the large area of positive SSSA in the GOA as well as positive SSSA along the GOA coastline. Freshening along the U.S. coastline north of about 40°N is driven by Ekman pumping, although anomalous horizontal salinity advection

(a) PDO   Offshore Volume Transport

(b) NPGO   Offshore Volume Transport

positive values (white contours)– offshore
negative values (black contours)- onshore

(c) Difference in offshore volume
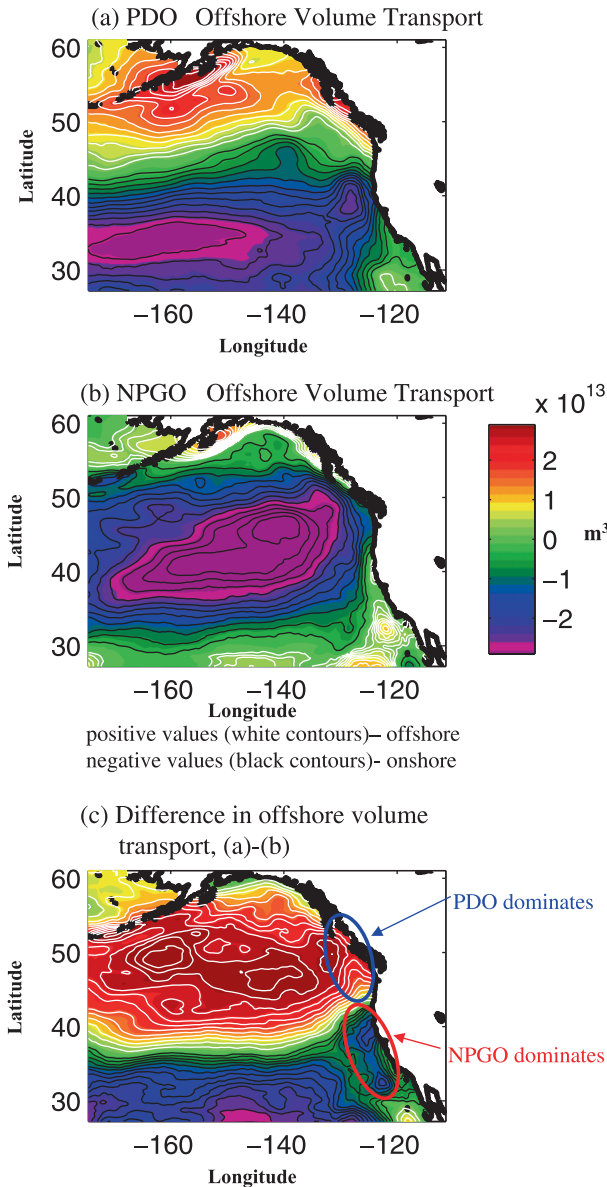transport, (a)-(b)

FIG. 9. Regression maps of the offshore volume transport for the (a) PDO and (b) NPGO based on anomalous ageostrophic currents where white contours indicate volume transport away from the coast and black contours indicate volume transport toward the coast. (c) The difference in these regression maps is shown, where white contours indicate that the volume transport associated with the PDO dominates while black contour lines indicate that the volume transport associated with the NPGO dominates.

contributes to a stronger salinification component. South of 40°N along the coast, Ekman pumping is weak and salinity anomalies are shaped by both mean and anomalous horizontal advection of SSSAs. The role of mean Ekman pumping (Fig. 8f) in driving NPGO SSSA is relatively small and does not impact S'_{NPGO}.

c. The role of ageostrophic currents

The results of this SSS budget analysis show that vertical advection via Ekman pumping does not play a significant role in influencing the variance in SSS along the coastline especially in the vicinity of the CCS. However, based on the Di Lorenzo et al. (2008), we know that coastal upwelling is important in this region. To reconcile this difference, we investigate the potential role of offshore volume transport caused by ageostrophic currents. A net volume transport away from the coast is an indicator of coastal upwelling and can contribute to variances in coastal SSS. To this end, the anomalous wind-driven zonal and meridional currents were decomposed into their respective geostrophic and ageostrophic components and rotated such that the zonal (offshore) component is normal to the U.S. coastline. As in section 3, the offshore ageostrophic velocities, denoted u_{ageo}, were regressed with the PDO and NPGO index yielding characteristic spatial patterns of u_{ageo} that are tied to each climate mode. An index of Ekman offshore transport was then computed using

$$\frac{1}{\alpha} \iint u_{ageo} dx dy, \qquad (6)$$

where dx and dy define the surface area of the model grid points. In (6), a positive volume transport will be away from the coast while a negative volume transport will be toward the coast. Figures 9a,b show the offshore volume transport associated with each climate mode, respectively, and indicate that along the coast, coastal upwelling via anomalous offshore ageostrophic flow is latitudinally nonuniform in both cases. By taking the difference between these modal volume transports (Fig. 9c), we find that coastal offshore volume transport north of about 40°–45°N is dominated by the PDO, while south of this latitude band the NPGO dominates. These results are consistent with the studies of Chhak and Di Lorenzo (2007) and Di Lorenzo et al. (2008), which use adjoint passive tracer experiments to investigate decadal changes of coastal upwelling in the CCS.

5. Shaping of the PDO and NPGO modes

In the previous section, we found that anomalous horizontal advection of mean gradients (i.e., $\mathbf{u}' \cdot \nabla \bar{T}$ and $\mathbf{u}' \cdot \nabla \bar{S}$) influence the basinwide spatial patterns of SSTAs and SSSAs associated with each climate mode more than any other physical process described by the surface temperature and salinity budgets [(4) and (5)]. Note that mean horizontal advection of anomalous SSSAs (i.e., $\bar{\mathbf{u}} \cdot \nabla S'$), however, also contributes significantly to the basinwide spatial pattern of SSSAs for the NPGO. This suggests that horizontal advection is the
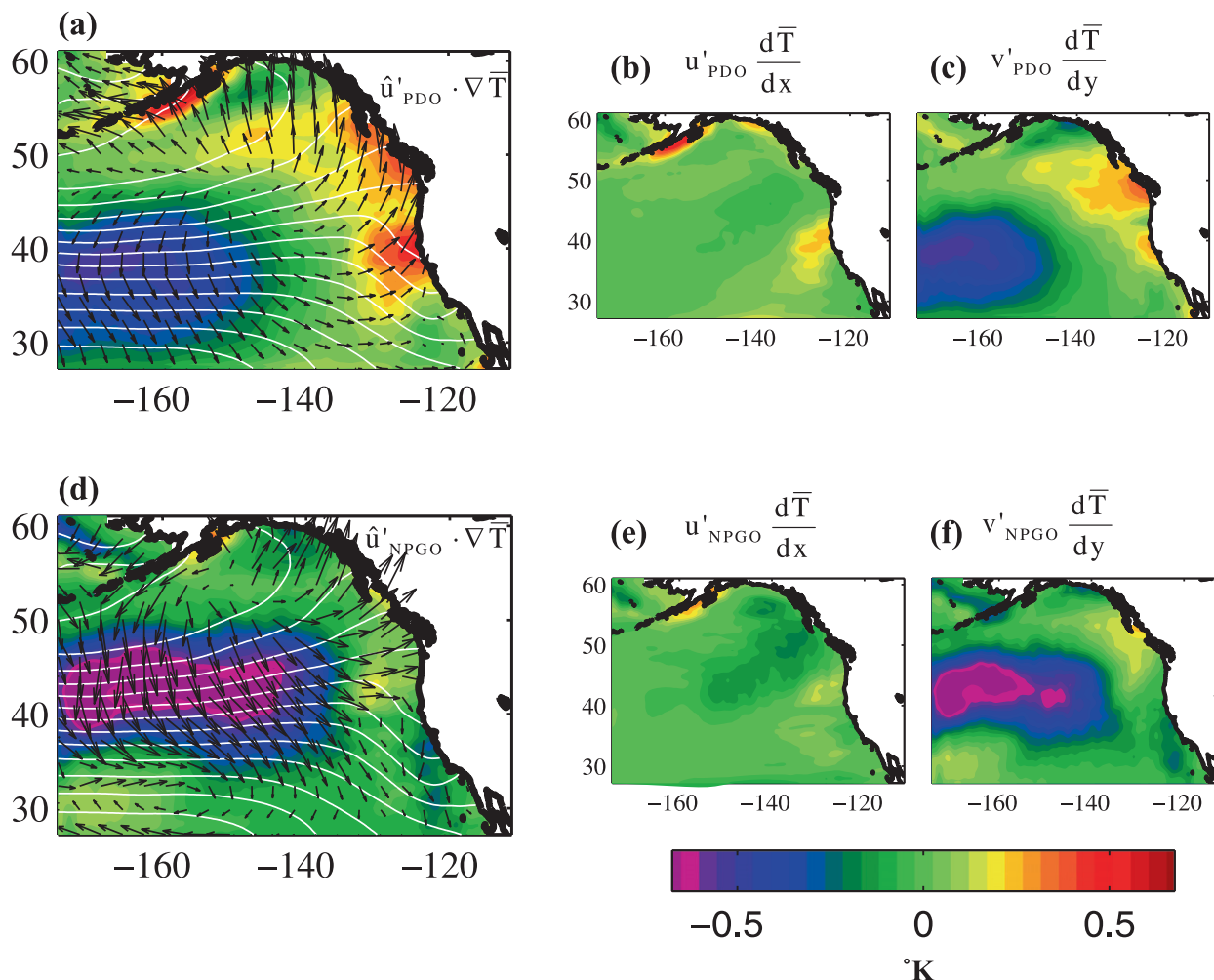
FIG. 10. The (b),(e) horizontal and (c),(f) meridional components of the SST budget term that describes anomalous horizontal advection of mean SST gradients for the (a) PDO and (b), NPGO, respectively. White contours in (a) and (d) are the mean SST gradients and black arrows are the anomalous surface currents associated with the PDO and NPGO.

key underlying dynamical process that shapes the large-scale spatial patterns associated with each of the climate modes. Other physical processes defined in (4) and (5) tend to contribute much less to the large-scale patterns associated with each mode and instead contribute more to smaller-scale patterns along the coast where we showed the reconstruction of the modes was sometimes less skillful. As shown previously, this area is also influenced by coastal upwelling induced by anomalous offshore ageostrophic currents. In this section, we are interested in understanding how the large-scale patterns associated with each mode are shaped. As such, we will concentrate *only* on the horizontal advection terms from our budget analysis described in the last section. We examine both the zonal and meridional components of the horizontal advection terms in (4) and (5) in order

to determine how each mode acquires the large-scale SSTA and SSSA patterns shown in Figs. 1e–h.

Figures 1e,f show that the large-scale SSTA pattern associated with each mode differs significantly from each other, with the PDO SSTA characterized by a monopole structure and the NPGO SSTA characterized by a dipole. Because anomalous horizontal advection of mean SST $\mathbf{u}' \cdot \nabla \bar{T}$ is the primary physical process that contributes to the large-scale structure of these patterns *and* $\nabla \bar{T}$ is the same for both modes, it is the anomalous wind-driven currents $\mathbf{u}'$ (black vectors on Figs. 1e,f) associated with each mode that causes the SSTA patterns to differ between the PDO and NPGO. These anomalous Ekman currents are driven by the atmospheric forcing patterns associated with each mode that are shown in Fig. 4. Figure 10 shows the zonal

(Figs. 10b,e) and meridional (Figs. 10c,f) components of $\mathbf{u}'_I \cdot \nabla \bar{T}$ (Figs. 10a,d) for both modes (either $I \equiv \text{PDO}$ or $I \equiv \text{NPGO}$) and indicates that it is primarily the anomalous *meridional* component of Ekman currents (v'_I) acting on the mean SST gradients (white contours on Figs. 10a,d) that shapes the large-scale SSTA patterns of each mode. Indeed, Figs. 1e,f show that where anomalous wind-driven Ekman currents (black arrows) appear to have a stronger meridional component, the SSTA tends to be stronger for both modes.

Recall that anomalous horizontal advection of mean SSS, $\mathbf{u}' \cdot \nabla \bar{S}$, is also the primary physical process that contributes to the large-scale SSSA patterns of each mode shown in Figs. 1g,h. Again, because $\nabla \bar{S}$ is the same for both modes, it must be the above-mentioned anomalous wind-driven Ekman currents $\mathbf{u}'_I$ driven by the atmospheric forcing patterns in Fig. 4 that cause the SSSA patterns to differ between the PDO and the NPGO. Because the shape of mean SSS contours (white contours on Figs. 1g,h) also differ from the shape of mean SST contours (white contours on Figs. 1e,f), anomalous horizontal advection of each also results in each mode's SSSA pattern being qualitatively very different from their corresponding SSTA pattern. The mean SST contours are mostly zonal basinwide, whereas the mean SSS contours are characterized by a monopole in the northern GOA and zonal contours in the interior of the basin that start to slope and become more meridional in the southeastern part of the basin. This has implications for how anomalous horizontal advection shapes the PDO and NPGO as we discuss next.

Figure 11 shows the zonal (Figs. 11b,e) and meridional (Figs. 11c,f) components of $\mathbf{u}' \cdot \nabla \bar{S}$ (Figs. 11a,d) for each mode and again indicates that the anomalous *meridional* component of Ekman currents (v'_I) tend to be most influential in shaping the basinwide SSSA patterns associated with each mode. The anomalous zonal component of Ekman currents ($\mathbf{u}'_I$) (Figs. 11b,e), however, also help shape the modes in various places in the basin where anomalous Ekman currents (black arrows, Figs. 11a,d) cross over mean SSS contours (white contours, Figs. 11a,d) that are more oriented in the north–south direction. Because mean SST contours are primarily zonal, the anomalous zonal component of Ekman currents was less important in shaping each mode's SSTA.

As mentioned, mean horizontal advection of SSSAs ($\bar{\mathbf{u}} \cdot \nabla S'$, Fig. 11g) also drives the NPGO SSSAs in the southwestern part of the GOA and is due to the large area of strong SSSA gradients in this region (white contours, Fig. 11g). Figure 11 shows the zonal (Fig. 11h) and meridional (Fig. 11i) components of this budget term for the NPGO. In this case, it is primarily the mean

meridional wind driven Ekman currents $\bar{v}$ that are most important (Fig. 11i) because they cross over the large area of strong SSSA gradients. The mean horizontal advection of SSSA for the PDO is not important because such strong SSSA gradients do not exist for large areas of the domain (white contours, Fig. 7e). This is also true for each mode's SSTA gradients (white contours, Figs. 5e and 6e) such that mean horizontal advection of SSTA for both modes does not contribute to shaping of the SSTAs of the modes.

To summarize, the large-scale basinwide patterns associated with each mode are shaped primarily by anomalous wind-driven ocean currents. These anomalous Ekman currents differ significantly between the PDO and NPGO because of the anomalous atmospheric forcing pattern associated with each mode. The PDO is forced by an atmospheric monopole anomaly, while the NPGO is forced by a dipole anomaly. Because of the position of the anomalous atmospheric monopole and dipole relative to mean SST and SSS gradients, anomalous Ekman currents with a strong meridional component are more influential than those with a strong zonal component in shaping the PDO and NPGO patterns. Mean meridional Ekman currents acting on very strong SSSA gradients in the southern GOA, however, are also important in shaping the SSSA of the NPGO.

6. Vertical expression of PDO and NPGO modes

In the previous section, we showed how the basinwide patterns of the PDO and NPGO mode are shaped by horizontal advection described in (4) and (5). In this section, we examine the vertical expressions of the PDO and NPGO. Figure 12 shows meridional and zonal cross sections of temperature and salinity anomalies associated with the PDO and NPGO. The first cross section is taken along 150°W, while the second is taken along 37°N, as indicated in the left-hand panels of Fig. 12. Overall, we find that the strong surface expressions of the PDO and NPGO extend only to about 200–250 m deep in the water column indicating that these climate modes are largely confined to the upper ocean.

The meridional (north–south) cross section of temperature anomalies of the PDO (Fig. 12a) indicates that the region of strong positive temperature anomalies in the northern GOA near the coast is shallower than the negative temperature anomalies to the south. Here, the negative SSTAs from the south are actually submerged underneath the shallow region of positive temperature anomalies. The same cross section of the NPGO (Fig. 12c) also indicates that temperature anomalies become shallower in the northern GOA. In addition to the shallow
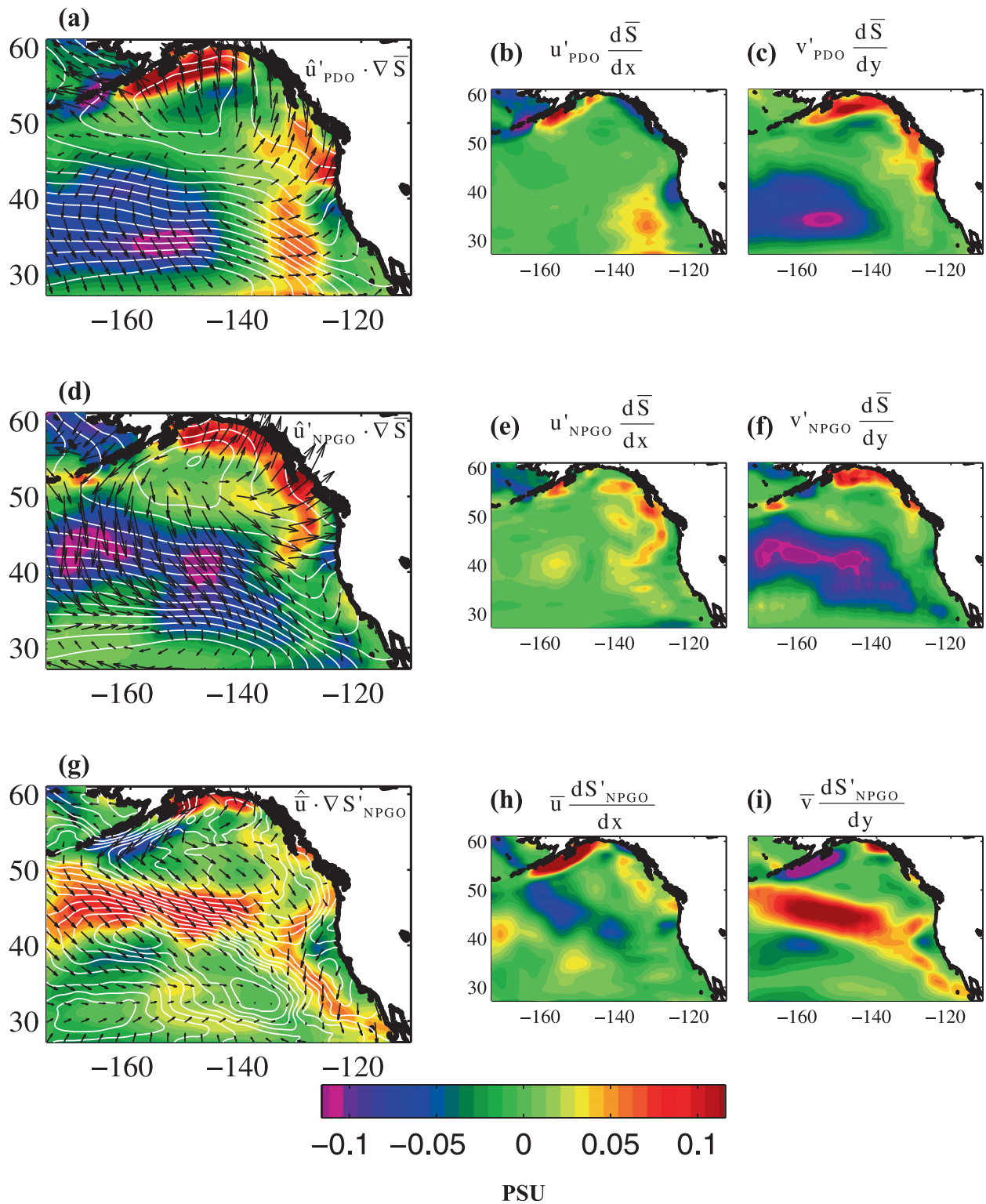
FIG. 11. As in Fig. 10, but for the SSS. Also shown are the (h) horizontal and (i) meridional components of the SSS budget term that describes mean horizontal advection of (g) anomalous SSS gradients for the NPGO. White contours in (g) are the anomalous SSS gradients associated with the NPGO and black arrows are the mean surface currents.
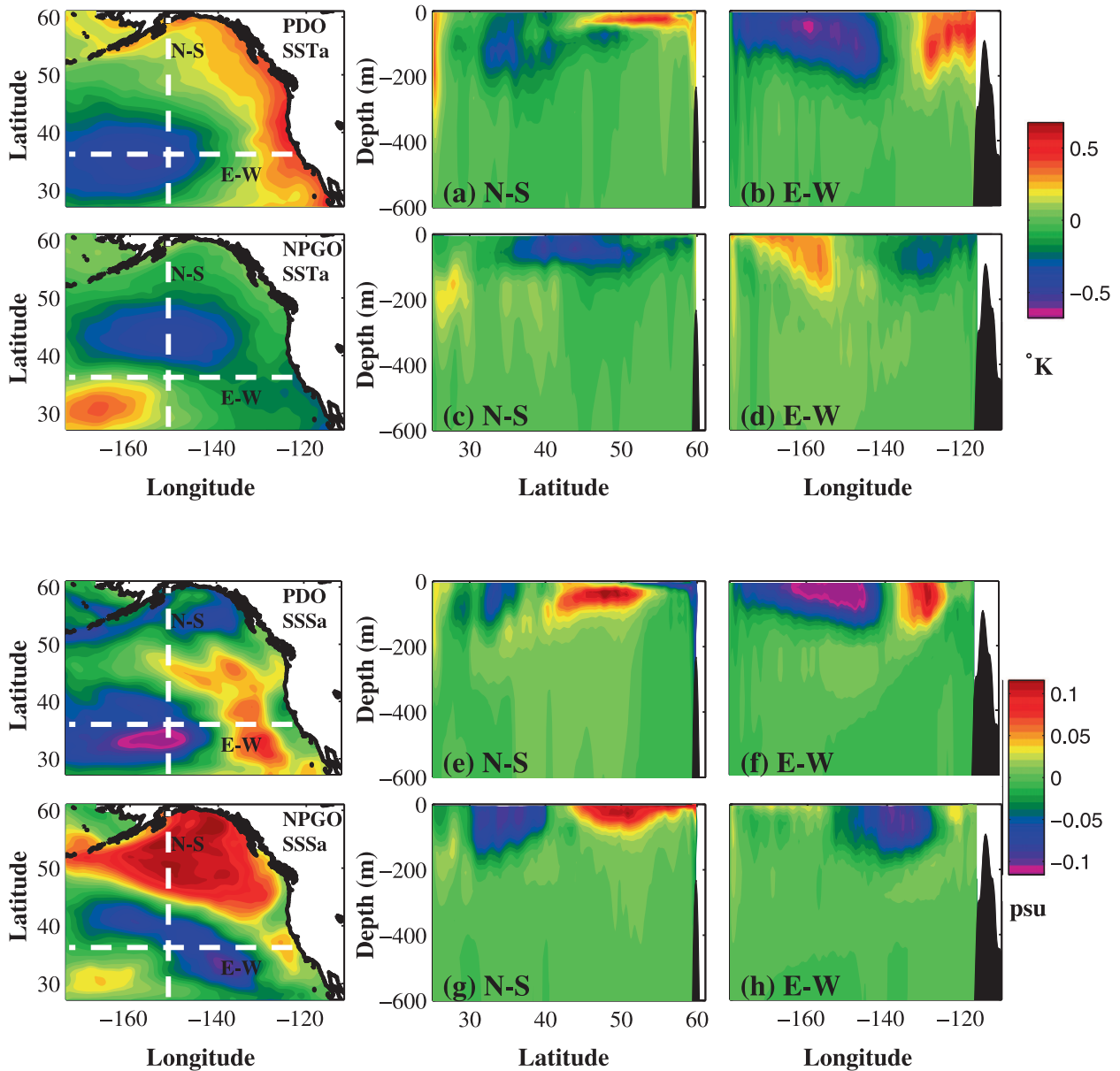
FIG. 12. Two vertical cross sections each of temperature and salinity anomalies associated with the (tops of each panel) PDO and (bottoms of each panel) NPGO. (a),(c),(e),(g) First cross section (north–south) taken along 150°W and (b),(d),(f),(h) second cross section (east–west) taken along 37°N , as indicated in the left panels of Fig. 9.

temperature signature of the PDO and NPGO in the northern GOA, this region also has a very shallow mixed layer depth (<40 m) and undergoes wintertime temperature inversions within the first 50 m. These factors lead to difficulties in specifying the "correct" vertical temperature gradient important in estimating the contributions of the Ekman pumping term in (4). This provides yet another explanation as to why the model SSTA budget reconstruction has less skill in this region, as previously noted in section 4a. The zonal (east–west) cross section of

temperature anomalies of the PDO (Fig. 12b) and NPGO (Fig. 12d) suggest that the surface expression of both modes is deepest (~250 m) in the interior of the basin. This is supported by the southern portion of the above-mentioned meridional cross sections (Figs. 12a,c).

The meridional cross section of salinity anomalies for the PDO (Fig. 12e), like the temperature anomalies, tends to be shallowest in the GOA. In the GOA, a shallow layer of freshwater lays above a slightly thicker layer of salty water. Although the model salinity profiles

do not exhibit seasonal dependence in the GOA, the shallowness of the salinity expression and mixed layer here may contribute to errors in the SSSA reconstruction in this region (Fig. 7b). The meridional cross section of salinity anomalies for the NPGO (Fig. 12g) indicate that the salinity surface expression is not as shallow in the GOA as compared to the previously discussed vertical profiles, and interestingly the SSSA reconstruction also has better skill in this region (Fig. 8b) when compared to the reconstruction of the PDO SSTA and SSSA and NPGO SSTA. This suggests that where the anomalies associated with the PDO and NPGO are shallow (deeper), the budget reconstructions are less (more) skillful. This is supported by the zonal cross sections of salinity anomalies for the PDO (Fig. 12f) and the NPGO (Fig. 12h), which show that the depth of salinity surface expressions is shallower close to the California coast where our SSS reconstructions were less skillful and deeper in the interior where the reconstructions were better.

7. Summary and discussion

In this paper, use has been made of a 55-yr integration of a model of the northeast Pacific to study the dominant low-frequency upper-ocean variability over the region. This variability is defined in terms of the two leading empirical modes of SSHA. A comparison with satellite altimeter data shows that there exists a close correspondence between these modes and the observed SSH variability. The first mode corresponds to the well-known PDO and has a monopole structure over the North Pacific resulting in strong coherent signals along the North American coastline. The second mode, termed the North Pacific Gyre Oscillation (NPGO), has a dipole pattern and is associated with the intensification and weakening of the eastern and central branches of the two gyres in the North Pacific. The NPGO has been shown (Di Lorenzo et al. 2008; DIL) to be highly correlated with important biological parameters in the northeast Pacific. This is consistent with the fact that the model NPGO accounts for the most variance in the model SSS.

While the PDO's monopole pattern has been shown to be related to the atmospheric Aleutian low, we find that the NPGO is likely related to the dipole structure associated with the so-called North Pacific Oscillation introduced by Walker and Bliss (1932). We were able to reconstruct the model NPGO index using a simple model for the NPGO index that is governed by an AR-1 process and forced by north–south gradients of sea level pressure anomalies (SLPAs) in the central NEP. This highlights the importance of atmospheric forcing in the

North Pacific for driving the low-frequency variability of the NPGO. Note that the two atmospheric forcing patterns associated with the PDO and NPGO, the Aleutian low and the NPO, respectively, are two distinct patterns (Bond et al. 2003; Peterson and Schwing 2003). By analyzing the budget terms that contribute to variations in SST and SSS for each mode, we are able to address the following questions:

1) *What is the relative importance of vertical advection via Ekman pumping versus wind-driven horizontal advection of ocean gradients?*

Anomalous horizontal advection of mean ocean gradients, particularly the anomalous alongshore component, is more influential in driving *basinwide* variations in SST and SSS than anomalous Ekman pumping. The latter, however, is important at various locations in the domain and it is important to variations of SST and SSS in the GOA, and to variations of SST in the CCS. Ekman pumping does *not*, however, contribute significantly to variations of SSS in the CCS. These results are mirrored in several other studies. Chelton and Davis (1982) also use the idea of anomalous alongshore advection to explain low-frequency salinity variations and Schneider et al. (2005) use long-term hydrographic observations in the Southern California Bight to show that salinity variability results from anomalous alongshore advection, which accumulates salinity anomalies along the equatorward path of water in the California Current. Schneider et al. (2005) also suggest that the ratio of horizontal to vertical advection in the Southern California Current is indeed larger for salinity than for temperature, which is consistent with our results that indicate that anomalous Ekman pumping has the greatest impact on SST in the CCS, rather than on SSS. We also show that coastal upwelling resulting from anomalous offshore ageostrophic currents plays a role in influencing SSS variance.

2) *Are the dynamics that control these modes uniform in the domain or are different local regions controlled by different dynamics and atmospheric forcings?*

The results show clearly that the atmospherically driven ocean dynamics are not uniform in the domain. Different dynamical processes are responsible for each modes′ SSTA and SSSA in different regions of the domain. Let us consider three main regions in the domain: the CCS, the GOA, and the central region of the domain that excludes the two above-mentioned regions. SSTAs in the CCS are driven by anomalous lateral advection and Ekman pumping, whereas SSSAs in the CCS are driven almost

exclusively by anomalous lateral advection. Note that lateral advection is tied to coastal upwelling. In the GOA, variations in the SST and SSS of both modes are forced by a combination of anomalous lateral advection and Ekman pumping and, additionally, the variations in SST are forced by anomalous net surface heat fluxes. In the central part of the domain, south of the GOA, variations in SST for both modes are controlled by both lateral advection and Ekman pumping, whereas variations in SSS are controlled only by lateral advection.

Each of the regions discussed here have their own unique mean circulations and it is clear that this influences how the ocean responds to the atmospheric forcing. Though the PDO and NPGO certainly have large-scale projections as seen in Fig. 4, the ocean response in the NEP clearly varies throughout the domain resulting from the different, spatially complex physical processes induced by the atmospheric forcing. As such, higher-resolution budget analyses of these different regions could prove more illuminating, but are beyond the scope of this paper. Further work examining the impact of these climate regimes on the complex eastern boundary currents is currently underway and will be reported elsewhere.

3) *Why does salinity select the NPGO as the dominant mode?*

It is counterintuitive that the PDO explains the most variance in the model SST and SSH but not the model SSS. Most variance in the model SSS is explained by the NPGO. The primary reason for this stems from the shape of the mean SSS gradients versus the mean SST gradients and the significantly different atmospheric forcing patterns tied to each mode. Mean SST gradients are mostly oriented in the zonal (east–west) direction. In contrast, the mean SSS pattern is dominated by a large-scale coherent pattern that is strongest in the northern part of the domain in the GOA. This results in areas of zonally and meridionally oriented mean SSS gradients. The anomalous surface currents of each mode are oriented such that those associated with the PDO have the largest impact on the zonal mean SST gradients, while those associated with the NPGO have the largest impact on the mean SSS gradients. As such, anomalous meridional *and* zonal advection are important for shaping the large-scale SSS pattern of the NPGO. Ekman pumping of mean salinity and mean horizontal advection of SSSA gradients also help explain why the NPGO is the dominant mode for salinity. Di Lorenzo et al. (2008; DIL) show that the NPGO does indeed capture more of the observed

decadal fluctuations in salinity than the PDO. It is also shown that this new climate mode is highly correlated with long-term observations of various nutrients and chlorophyll-a Di Lorenzo et al. (2008; DIL).

The results of this work demonstrate that the NPGO must be considered in addition to the PDO regarding NEP climate variability. While the climate shift of 1977 is primarily associated with the PDO (Miller et al. 1994a; Hare and Mantua 2000; McGowan et al. 2003), the NPGO also plays an important role in the climate shift after 1990 (Bond et al. 2003). It is likely that the dipole pattern of the NPGO will reflect north/south coastal variations (Bond et al. 2003), and therefore may serve as an additional index to the PDO for understanding ecological conditions along the western coast of North America.

REFERENCES

Barnett, T., and R. Preisendorfer, 1987: Origins and levels of monthly and seasonal forecast skill for United States surface air temperatures determined by canonical correlation analysis. *Mon. Wea. Rev.,* **115,** 1825–1850.

Bond, N. A., J. E. Overland, M. Spilane, and P. Stabeno, 2003: Recent shifts in the state of the North Pacific. *Geophys. Res. Lett.,* **30,** 2183, doi:10.1029/2003GL018597.

Capet, X. J., P. Marchesiello, and J. C. McWilliams, 2004: Upwelling response to coastal wind profiles. *Geophys. Res. Lett.,* **31,** L13311, doi:10.1029/2004GL020123.

Capotondi, A., M. Alexander, C. Deser, and A. Miller, 2005: Low-frequency pycnocline variability in the northeast Pacific. *J. Phys. Oceanogr.,* **35,** 1403–1420.

Chavez, F., J. Ryan, S. Lluch-Cota, and M. Ñiquen, 2003: From anchovies to sardines and back: Multidecadal change in the Pacific Ocean. *Science,* **299,** 217–221.

Chelton, D. B., and R. E. Davis, 1982: Monthly mean sea-level variability along the west coast of North America. *J. Phys. Oceanogr.,* **12,** 757–784.

Chhak, K., and E. Di Lorenzo, 2007: Decadal variations in the California Current upwelling cells. *Geophys. Res. Lett.,* **34,** L14604, doi:10.1029/2007GL030203.

Crawford, W., J. Galbraith, and N. Bolingbroke, 2007: Line P ocean temperature and salinity, 1956–2005. *Prog. Oceanogr.,* **75,** 161–178.

Cummins, P. F., and G. S. E. Lagerloef, 2004: Wind-driven inter-annual variability over the northeast Pacific Ocean. *Deep-Sea Res. I,* **51,** 2105–2121.

——, ——, and G. Mitchum, 2005: A regional index of northeast Pacific variability based on satellite altimeter data. *Geophys. Res. Lett.,* **32,** L17607, doi:10.1029/2005GL023642.

Curchitser, E. N., D. B. Haidvogel, A. J. Hermann, E. L. Dobbins, T. M. Powell, and A. Kaplan, 2005: Multi-scale modeling of the North Pacific Ocean: Assessment and analysis of simu-lated basin-scale variability (1996–2003). *J. Geophys. Res.,* **110,** C11021, doi:10.1029/2005JC002902.

Davis, R., 1976: Predictability of sea surface temperature and sea level pressure anomalies over the north Pacific ocean. *J. Phys. Oceanogr.,* **6,** 249–266.

Dawe, J., and L. Thompson, 2007: PDO-related heat and tem-perature budget changes in a model of the North Pacific. *J. Climate,* **20,** 2092–2108.

Di Lorenzo, E., 2003: Seasonal dynamics of the surface circulation in the southern California current system. *Deep-Sea Res. II,* **50,** 2371–2388.

——, A. Miller, N. Schneider, and J. McWilliams, 2005: The warming of the California current: Dynamics and ecosystem implications. *J. Phys. Oceanogr.,* **35,** 336–362.

——, and Coauthors, 2008: North Pacific gyre oscillation links ocean climate and ecosystem change. *Geophys. Res. Lett.,* **35,** L08607, doi:10.1029/2007GL032838.

Graham, N., 1994: Decadal scale variability in the 1970's and 1980's: Observations and model results. *Climate Dyn.,* **10,** 60–70.

Haidvogel, D., H. Arango, K. Hedstrom, A. Beckmann, P. Malanotte-Rizzoli, and A. Shchepetkin, 2000: Model eval-uation experiments in the north Atlantic basin: Simulation in nonlinear terrain following coordinates. *Dyn. Atmos. Oceans,* **32,** 239–281.

——, and Coauthors, 2008: Regional ocean forecasting in terrain-following coordinates. *J. Comput. Phys.,* **227,** 3595–3624.

Hare, S., and N. Mantua, 2000: Empirical evidence for North Pacific regime shifts in 1977 and 1989. *Prog. Oceanogr.,* **47,** 103–145.

Hasselmann, K., 1976: Stochastic climate models. Part I. Theory. *Tellus,* **28,** 473–485.

Lagerloef, G. S. E., 1995: Interdecadal variations in the Alaska gyre. *J. Phys. Oceanogr.,* **25,** 2242–2258.

Latif, M., and T. Barnett, 1994: Causes of decadal climate varia-bility over the North Pacific and North America. *Science,* **266,** 634–637.

Levitus, S., R. Burgett, and T. Boyer, 1994: *Salinity.* Vol. 3, *World Ocean Atlas 1994,* NOAA Atlas NESDIS 3, 99 pp.

Mantua, N., S. Hare, Y. Zhang, J. Wallace, and R. Francis, 1997: A Pacific interdecadal climate oscillation with impacts on salmon production. *Bull. Amer. Meteor. Soc.,* **78,** 1069–1079.

Marchesiello, P., J. C. McWilliams, and A. Shchepetkin, 2003: Equilibrium structure and dynamics of the California Current System. *J. Phys. Oceanogr.,* **33,** 753–783.

McGowan, J., S. Bograd, R. Lynn, and A. Miller, 2003: The bio-logical response to the 1977 regime shift in the California Current. *Deep-Sea Res. II,* **50,** 2567–2582.

Miller, A., D. Cayan, T. Barnett, N. Graham, and J. Oberhuber, 1994a: The 1976–77 climate shift of the Pacific Ocean. *Oceanography,* **7,** 21–26.

——, ——, ——, ——, and ——, 1994b: Interdecadal variability of the Pacific Ocean: Model response to observed heat flux and wind stress anomalies. *Climate Dyn.,* **9,** 287–302.

Moore, A. M., H. G. Arango, E. Di Lorenzo, A. J. Miller, and B. D. Cornuelle, 2009: An adjoint sensitivity analysis of the southern California current circulation and ecosystem. *J. Phys. Oceanogr.,* in press.

Newman, M., G. P. Compo, and M. A. Alexander, 2003: ENSO-forced variability of the Pacific decadal oscillation. *J. Climate,* **16,** 3853–3857.

Peterson, W. T., and F. B. Schwing, 2003: A new climate regime in northeast Pacific ecosystems. *Geophys. Res. Lett.,* **30,** 1896, doi:10.1029/2003GL017528.

Rodionov, S., J. Overland, and N. Bond, 2005: The Aleutian low and winter climatic conditions in the Bering Sea. Part I: Classification. *J. Climate,* **18,** 160–177.

Schneider, N., and B. Cornuelle, 2005: The forcing of the Pacific decadal oscillation. *J. Climate,* **18,** 4355–4373.

——, E. D. Lorenzo, and P. Niiler, 2005: Salinity variations in the southern California Current. *J. Phys. Oceanogr.,* **35,** 1421–1436.

Shchepetkin, A., and J. McWilliams, 2004: The regional oceanic modeling system (ROMS): A split explicit, free-surface, topography-following-coordinate oceanic model. *Ocean Modell.,* **9,** 347–404.

Smith, T., and R. Reynolds, 2004: Improved extended recon-struction of SST (1854–1997). *J. Climate,* **17,** 2466–2477.

Strub, P., and C. James, 2002: Altimeter-derived surface circula-tion in the large-scale NE Pacific gyres, Part 2: 1997–1998 El Niño anomalies. *Prog. Oceanogr.,* **53,** 185–214.

Trenberth, K., and J. Hurrell, 1994: Recent observed interdecadal climate changes in the Northern Hemisphere. *Climate Dyn.,* **9,** 303–319.

Walker, G., and E. Bliss, 1932: World weather V. *Mem. Roy. Meteor. Soc.,* **4,** 53–84.

Zhang, Y., 1996: An observational study of atmosphere-ocean in-teractions in the northern oceans on interannual and inter-decadal time-scales. Ph.D. thesis, University of Washington, 306 pp. [Available from University Microfilms, 1490 Eisenhower Place, P.O. Box 975, Ann Arbor, MI 48106.]

——, J. Wallace, and D. S. Battisti, 1997: ENSO-like interdecadal variability. *J. Climate,* **10,** 1004–1020.